

## Quantum-Mechanical Calculations of Resonance Raman Intensities: The Weighted-Gradient Approximation

Andrzej A. Jarzęcki\*

Department of Chemistry, Brooklyn College and the Graduate School of the City University of New York, Brooklyn, New York 11210

Received: October 29, 2008; Revised Manuscript Received: January 9, 2009

A framework of the weighted-gradient approach is developed for effective quantum-mechanical modeling of resonance Raman (RR) intensities with a view toward rationalizing enhancement patterns observed for histidine and tryptophan side chains. Unlike the single-state gradient approach, this new procedure utilizes the vertical gradients obtained for all computed excited states to produce an effective gradient and the RR intensity patterns for a particular frequency of the excitation photon. The dramatic spectral changes observed for the histidine ring upon its protonation, deprotonation, or deuterium substitution of exchangeable protons is well reproduced by this model. Spectral comparison for the tryptophan ring clearly demonstrated improved quality of the weighted-gradient over the single-state gradient approach. Computed spectra exemplify the potential application of this model to support vibrational studies of electronic and structural interactions of chromophores in proteins.

### Introduction

Among the various analytical probes used to investigate a wide range of important biological or environmental processes, resonance Raman [RR] spectroscopy is capable of providing particularly useful data because of the sensitivity of vibrational frequencies to molecular structure and the electronic sensitivity conferred by resonance enhancement. This sensitivity makes it possible to do small molecule spectroscopy inside large molecules and extract structural details for key molecular fragments at biologically active sites or detect dynamics of the surrounding macromolecules.<sup>1,2</sup> For instance, the analytical utility of resonance Raman excitations in the far ultraviolet region becomes a significant source of spectroscopic information on the conformation, hydrogen bonding, hydrophobic interactions, metal coordination, and so forth of protein main chains and aromatic amino acid side chains.<sup>2</sup> Among aromatic amino acids, histidine and tryptophan are particularly important protein residues. Tryptophan gives the strongest RR signals<sup>3</sup> which were successfully applied to study protein environments. The histidine side chain is frequently involved in catalysis and ligation of essential metal ions, but the UVR enhancement of its vibrations is weak.<sup>4</sup> Nevertheless, when supported by computational and experimental spectra–structure correlations, certain signals of histidine could be detectable in proteins.<sup>5–7</sup>

The sensitive spectroscopic data available via resonance Raman for small molecular fragments of macromolecules naturally presents a unique possibility to employ state-of-the-art advanced computational methods to predict and support these experiments with theoretical insights and calibrate or test the accuracy of existing or newly developed theoretical methods. Quantum-mechanical calculations of IR and nonresonance Raman spectra have been remarkably successful in prediction of vibrational frequencies and intensities, greatly reducing ambiguities in mode assignments for compounds of the size of metalloporphyrins<sup>8</sup> or larger. However, a reliable prediction of resonance Raman intensity patterns proved to be computationally

more demanding because modeling of the enhancement is subject to accurate assessment of propagation of the ground-state wave function on the potential-energy surface of the resonant excited state or states.

Most quantum-mechanical methods capable of predicting RR intensity patterns for biologically significant chromophores cannot use the “traditional”, computationally demanding, sum-over-states formalism.<sup>9</sup> Instead, the calculations utilize approximations that originate from the single-state time-dependent formalism developed by Heller and co-workers<sup>10</sup> often in combination with transform methods for empirical corrections such as the Kramers–Kronig transform of an experimental absorption spectrum.<sup>11</sup> The most commonly used methods, the displacement<sup>12</sup> and gradient<sup>13</sup> approximations, were moderately successful, but their general success in predicting observed intensity patterns was sometimes questionable. Most recent developments to improve on the reproducibility of experimental RR intensities and excitation profiles focus on derivations of new relations to evaluate the time-dependent wave packet overlap in the case of frequency changes between the ground and excited states, incorporation of inhomogeneous broadening effects,<sup>14</sup> and solvent effects.<sup>15</sup> Other electronic parameters such as Duschinsky rotations,<sup>16</sup> anharmonicities, overtones, and nonadiabatic effects of electronic transitions were also investigated. Interestingly, Schatz and co-workers<sup>17</sup> developed an alternative approach which effectively evaluates resonance Raman scattering from the geometrical derivatives of the frequency-dependent polarizability by including a finite lifetime of electronic excited states using TD-DFT. This method could be considered as an attractive option for large molecules, although inherently limited by many of the same approximations as used in the excited-state gradient approximation method.

In general, the key shortcomings of successful prediction of RR spectra using the current time-dependent formalism always recognize effects of close-lying excited states and the necessity to single out the state which is most likely in resonance with a particular laser excitation. Therefore, development of efficient procedures to predict which excited state or states might be most appropriate to obtain accurate enhancements for a particular laser

\* To whom correspondence should be addressed. E-mail: jarzecki@brooklyn.cuny.edu.

excitation and at the same time to make knowledgeable negligence of other electronic excitations could present the opportunity to study not only specific enhancements of molecular vibrations but also the complexity and specificity of resonance enhancement, and extend a conventional viewpoint of the state-specific approach to the photon-specific multistate approach.

Here, we present the refinement methodology to improve on the generally accepted gradient approximation of a propagation of the ground-state wave function on the resonant excited state that is generalized to look out for effects of close-lying excited states. Unlike the single-state gradient approximation, the refinement procedure utilizes a manifold of computed excitations in the UV spectral region to produce the weighted gradient which could be effectively evaluated for a particular excitation wavelength in the computed spectral region. Hence, in principle, it provides the quantum-mechanical means to compute not only RR intensity patterns but also the excitation profiles of vibrational bands. In addition, illustrative calculations of RR spectra for biologically relevant chromophores; a histidine residue with its various side chain forms and a tryptophan side chain, are presented here to demonstrate the accuracy of the model and exemplify its potential application for molecular systems.

## Methodology

### Scattering Tensor and UVR Enhancement Mechanisms.

The theory of the resonance Raman scattering differentiates two major intensity enhancement mechanisms that play a dominant role in the RR spectra: (1) the Franck–Condon (F–C) scattering and (2) the Herzberg–Teller (H–T) vibronic coupling. The Franck–Condon mechanism is most pronounced for strongly allowed electronic transitions with large values of dipole moments ( $\mu_e^0$ ) and substantial magnitudes of the Franck–Condon integrals upon electronic excitation, such as electric-dipole allowed  $\sigma$ – $\sigma^*$ ,  $\pi$ – $\pi^*$ , and charge-transfer transitions. Excitations into a weak electronic transition such as forbidden  $\pi$ – $\pi^*$ , ligand field d–d, and spin forbidden transitions will not produce significant Franck–Condon scattering. On the other hand, Herzberg–Teller scattering is most pronounced when the exciting frequency is tuned to a weakly allowed electronic transition that is mixed vibronically with a nearby strong one. The Franck–Condon scattering mechanism is commonly expected and observed in RR spectra, while the Herzberg–Teller scattering becomes significant and is observed for specific molecular circumstances.<sup>18</sup>

Starting from the Kramers–Heisenberg dispersion equation and a Taylor series expansion of the transition dipole moment,  $\mu_e$ , along a vibrational normal coordinate,  $Q_k$ , in the adiabatic Born–Oppenheimer approximation both F–C and H–T mechanisms in resonance Raman scattering yields the following expressions for the components of the transition tensor<sup>9</sup>

$$[\alpha_{FC}]^{g \rightarrow f} = \frac{1}{h} \sum_e |\mu_e^0|^2 \sum_k \left[ \frac{\langle f^j | e^k \rangle \langle e^k | g^i \rangle}{\nu^{e,k} - \nu^{g,i} - \nu_o + i\Gamma^e} \right] \quad (1)$$

$$[\alpha_{HT}]^{g \rightarrow f} = \frac{1}{h} \sum_e \mu_e^0 \left( \frac{\partial \mu_e}{\partial Q_k} \right)_o \sum_k \left[ \frac{\langle f^j | Q_k | e^k \rangle \langle e^k | g^i \rangle + \langle f^j | e^k \rangle \langle e^k | Q_k | g^i \rangle}{\nu^{e,k} - \nu^{g,i} - \nu_o + i\Gamma^e} \right] \quad (2)$$

Hence, the quantum-mechanical prediction of the intensity patterns in the RR spectra resulting from the F–C mechanism

under conditions of resonance ( $\nu^{e,k} - \nu^{g,i} \cong \nu_o$ ) that is modulated by a damping factor ( $i\Gamma^e$ ) relies on accurate evaluation of the dipole moment of the electronic transition,  $\mu_e^0$ , and the Franck–Condon overlap integrals between the vibrational wave functions of the vibrational levels of the resonant excited state  $|e^k\rangle$  with the initial  $|g^i\rangle$  and final  $|f^j\rangle$  vibrational levels. For the fundamental Raman transition, the vibrational levels  $|f^j\rangle$  and  $|g^i\rangle$  are simply  $|g^1\rangle$  and  $|g^0\rangle$  of the ground electronic state. Unfortunately, explicit computation of the wave function propagation and the F–C integrals for most systems of chemical and biochemical interest exceeds a practical limit due to the size of the problem. Nevertheless, within the harmonic oscillator approximation and following Manneback's recursion formula,<sup>19</sup> it can be shown that the F–C integrals become nonzero for transitions between electronic states if there is a shift  $\Delta Q_k$  in the excited-state potential along the vibrational coordinate  $k$

$$\langle f^j | e^k \rangle \langle e^k | g^i \rangle = \Delta_k^e = \left( \frac{4\pi^2 \mu_k}{h} \right)^{\frac{1}{2}} \left( \frac{\nu_k^e \nu_k^g}{\nu_k^e + \nu_k^g} \right)^{\frac{1}{2}} \Delta Q_k \quad (3)$$

where  $\mu_k$  is the effective mass and  $\nu_k^e$  and  $\nu_k^g$  are vibrational frequencies of the  $k$ th vibrational mode for the resonant and ground electronic states. In this expression the evaluation of the F–C component of the transition tensor becomes accessible for more realistic molecular systems. Furthermore, assuming the displaced harmonic oscillator model<sup>20</sup> to approximate the resonant state potential by a shifted potential of the ground state,  $\nu_k^e \cong \nu_k^g$ , the equation for the  $\nu_k^e$  shift simplifies, and the structural change along the normal mode  $\Delta Q_k$  upon excitation of the molecule within Heller's time-dependent formulation<sup>10,13</sup> is easily linked to the gradient computed at the relevant resonant state or states in the Franck–Condon region

$$\Delta_k^e = \left( \frac{2\pi^2}{h} \right)^{\frac{1}{2}} \left\{ \left( \frac{\partial E_e}{\partial Q_k} \right) \sqrt{\mu_k \nu_k^g} \right\} \quad (4)$$

where the resonant state gradient,  $(\partial E_e / \partial Q_k)$ , vibrational force field of the ground state and the electronic transition dipole moment  $\mu_e^0$  is sufficient to compute the F–C component of the transition tensor,  $[\alpha_{FC}]^{g \rightarrow f}$ .

**Raman Intensities.** The RR intensity for F–C transition collected at  $\pi/2$  angle is proportional to the product of transition polarizability tensor with its complex conjugate and leads to

$$I_{k,FC}^{g \rightarrow f} \propto (\nu_o - \nu_k^g)^3 \nu_o \left| \sum_e |\mu_e^0|^2 \sum_k \left\{ \left( \frac{\partial E_e}{\partial Q_k} \right) \sqrt{\mu_k \nu_k^g} \right\} \left\{ \frac{\nu_o - \nu_k^g}{(\nu_o - \nu_k^g)^2 + \Gamma^2} + \frac{i\Gamma}{(\nu_o - \nu_k^g)^2 + \Gamma^2} \right\} \right|^2 \quad (5)$$

where each vibrational mode  $k$  is treated as an independent oscillator and the F–C overlap is evaluated within the gradient approximation. With a typical assumption of the short-time propagation<sup>10a</sup> of the ground-state vibrational wave function on the single, nondegenerate resonant state potential-energy surface, eq 5 for RR intensity simplifies to<sup>21,22</sup>

$$I_{k,FC}^{g \rightarrow f} \propto (v_o - v_k^g)^3 v_o |\mu_e^o|^4 \left( \frac{v_k^g}{\mu_k} \right) \left( \frac{\partial E_e}{\partial Q_k} \right)^2 \quad (6)$$

This gradient formulation of resonance Raman phenomena provides an attractive physical basis for the Raman scattering by connecting excited wave packet motion on the resonant state to the force at the vertical excitation. However, the limits of this single-state gradient formulation are clear when the resonant states of interest are degenerate or nearly degenerate. In these cases, the RR intensities are subject to interferences between closely spaced electronic components and their resonant contributions add or subtract at the amplitude level, significantly alternating the intensity patterns.

**Weighted-Gradient Correction.** In principle, the limitation of the single-state gradient formulation briefly described above can be easily corrected and extended to all computed states of the electronic absorption spectrum by introducing the weighted-gradient approximation, where each computed excited-state gradient is weighted by the appropriate  $W_{\Gamma,e}$  factor at the amplitude level as shown in eq 7

$$I_{k,FC}^{g \rightarrow f} \propto (v_o - v_k^g)^3 v_o \left( \frac{v_k^g}{\mu_k} \right) \sum_e \left| \left( \frac{\partial E_e}{\partial Q_k} \right) W_{\Gamma,e} \right|^2 \quad (7)$$

The equation distinguishes two key factors that modulate a gradient contribution at the amplitude level for a particular frequency of the excitation photon: (1) square of an electronic transition dipole moment  $|\mu_e^o|^2$  (oscillator strength of an electronic transition) and (2) the newly introduced weighting factors  $W_{\Gamma,e}$  which depend on the frequency of the incident light,  $v_o$ , and the energy offset  $\Gamma_e$  for a particular excited state. A natural choice for evaluating weighting factors  $W_{\Gamma,e}$  might be a Gaussian or a Lorentzian profile or a combination of these (a Voigt function). In the present study, a Lorentzian profile was chosen to compute the weighting factors according to the formula

$$W_{\Gamma,e} = \frac{|\mu_e^o|^2}{N} \left\{ \frac{\Gamma_e^2}{\Gamma_e^2 + (v_o - (v^{e,k} - v^{g,i}))^2} \right\} \quad (8)$$

where a particular electronic transition  $v^{e,k} - v^{g,i}$  is characterized by an empirically determined energy offset (damping parameter  $\Gamma_e$ ) and a proportionality constant  $N$  normalizes eq 8 so a full spectrum of computed weighting factors sum up to unity. Note that the equation is normalized at the amplitude level, therefore, the gradient amplitude of a particular excited state along a vibrational mode  $k$  contributing to its RR intensity is directly expressed as the fraction of the weighted gradient. Satisfactory demonstration of a correction for RR intensities that arise from near-degenerate resonant states were previously demonstrated for free-base porphyrins using the “effective force” approximation for the B excited states by weighting the computed closely spaced  $B_x$  and  $B_y$  state gradients by two adjustable factors,<sup>13b</sup> which is formally the case of a simple two-state weighted-gradient approximation.

Unlike the single-state gradient approximation, a new formulation of weighted gradients spans all frequencies of the computed electronic absorption and provides quantum-mechanical insight into the variation of resonance Raman intensity of the vibrational modes with excitation wavelength, a plot of which is known as an excitation profile.<sup>10b,23</sup> Such a plot tracks the absorption spectrum (electronic excitations) in a general way

but differs from it in detail, often revealing more structure. The excitation profile emphasizes electronic factors that are particularly sensitive to the mode under consideration, while the absorption shows no such selectivity. Consequently, the excitation profile of the vibrational modes can provide information about the excited state that may be hidden in the absorption spectrum.<sup>23</sup> The quantitative analyses of excitation profiles and RR intensities are of considerable general interest; however, experimentally they are limited to specific or relatively narrow frequency regions because of the constrained capacity to change laser excitations. In principle, computational modeling of the excitation profiles within the weighted-gradient approximation provides an effective tactic for quantum-mechanical exploration of electronic excitations.

The accuracy and reliability of computed RR spectra and excitation profiles within the weighted gradient approximation rely on the precision of predicted molecular properties such as the ground-state geometry, the ground-state vibrational force field, excited-state gradients, their oscillator strengths, and damping parameters,  $\Gamma$ , characterizing spectral profiles.

**Ground-State Geometry and Force Field.** Illustrative model calculations of the ground-state geometries, harmonic force constants, and frequencies were performed using density functional theory with the B3LYP nonlocal hybrid functional and moderate 6-31G\* basis sets as implemented in the Gaussian 03 suite of programs.<sup>24</sup> To improve the quality of the computed frequencies and normal modes, the computed models were imbedded in an aqueous environment mimicked by a polarizable cavity, i.e., the polarizable continuum model (PCM)<sup>25</sup> as implemented in Gaussian 03. It is important to point out that in this model the nature of solute–solvent interactions is purely electrostatic and any specific molecular interactions such as a possible formation of hydrogen bonds is excluded from calculations. Nevertheless, the PCM treatment has been successfully applied in the computation of numerous molecular properties including molecular geometries and harmonic force fields in various solvents, giving confidence in the predicted ground-state vibrational modes. When desired, even further refinement of PCM DFT force constants and frequencies might be easily accessible by employing scaling procedures such as the scaled quantum-mechanical (SQM) with transferable scaling factors<sup>26</sup> (see below). The line shapes for all computed vibrational spectra were simulated with 5 cm<sup>−1</sup> half-bandwidth Lorentzian profiles.

**Excited-State Gradients.** RR intensity prediction requires accurate estimation of excited-state gradients in the Franck–Condon region, although the excitation energies themselves need not be accurately computed. Good efficiency of prediction of the RR intensities was previously demonstrated for Ni porphyrins using the semiempirical ZINDO approximation,<sup>27</sup> and for imidazole and *N*-methylmesoporphyrin using the CIS (configuration interaction with single excitations)<sup>28</sup> and CASSCF<sup>29</sup> (multireference wave function) methods for selected electronic excited states. Recently developed time-dependent DFT methods<sup>30</sup> are dramatically increasing in popularity due to improved quality in computed excitation energies.<sup>13</sup> TD-DFT methods are an engaging choice to explore the accuracy of density functionals in predicting RR intensity patterns, however, fast analytical evaluation of TD-DFT excited-state gradients is not yet commonly implemented, and these gradients need to be calculated by numerical differentiation that increases the computational cost and could contain a certain amount of numerical noise resulting from finite convergence or other cutoffs. If analytical gradients are available, the calculations become particularly efficient since gradients are obtained at the computational cost



of a single excited-state calculation. The efficiency might be particularly significant when a large number of excited-state gradients need to be evaluated. Therefore, previously tested<sup>13a,b</sup> competence and easy access to analytically computed gradient as implemented in commonly available quantum chemical packages, makes the CIS approximation the most appealing choice for prediction of resonance Raman spectra for presented studies at this moment.

All model ultraviolet absorption spectra in this study were calculated based on evaluation of the 60 lowest electronic excitations from the computed PCM DFT ground-state geometry employing the CIS level of theory and 6-31G\* basis sets. In addition, the PCM procedure was employed for all evaluated excitations and excited-state gradients. Line shapes of computed UV spectra were simulated based on computed oscillator strengths and adoption of a Lorentzian band profile with a 0.350 eV half-bandwidth for each computed singlet–singlet excitation.

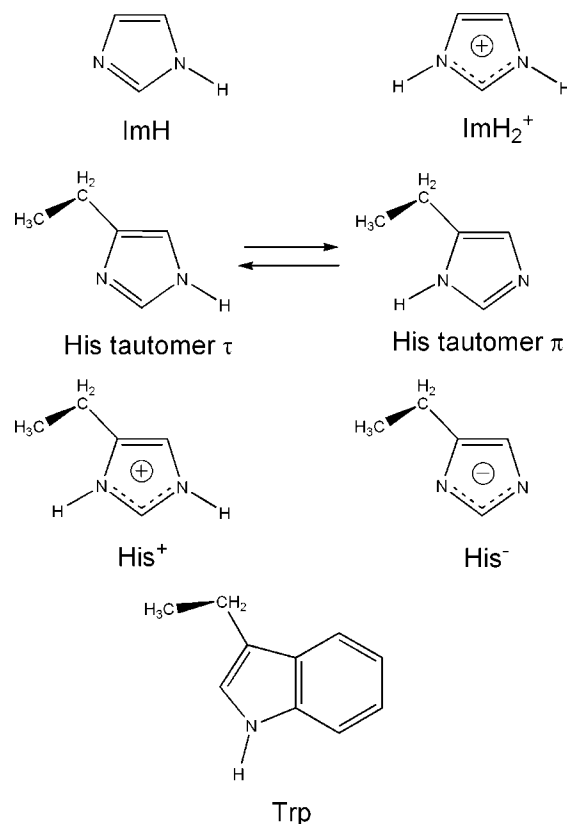
**Ground-State Gradient Correction.** A requirement for gradient correction in the similarly outlined calculations of RR intensities was already demonstrated for *N*-methylmesoporphyrin,<sup>13b</sup> and similar correction was employed to shift excited-state displacements relative to the ground-state equilibrium geometry.<sup>14</sup> When the excited-state gradients or their displacements are evaluated on different levels of theory than the equilibrium ground-state geometry (optimized gradients), the difference in the evaluated potentials introduces residue gradients or deterioration of displacements for which the excited states or displacements need to be corrected. In the RR calculations outlined here, the PCM CIS calculations involve excitations from a PCM HF reference potential, which does not produce the same ground-state equilibrium geometry as the PCM DFT potential. The corrected gradients are obtained according to

$$\left(\frac{\partial E_e}{\partial Q_k}\right)_{\text{corr}} = \left(\frac{\partial E_e}{\partial Q_k}\right)_{\text{CIS}} - \left(\frac{\partial E_e}{\partial Q_k}\right)_{\text{HF}} \quad (9)$$

where subscripts CIS and HF denote the computed PCM CIS and PCM HF gradients on the corresponding potential-energy surfaces along a normal coordinate *k* at the PCM DFT ground-state equilibrium geometry and the subscript corr indicates the corrected gradients. This correction is essential and has large effects on the computed intensities especially for low-frequency modes.

**Oscillator Strengths and Damping Parameters.** Generally, the line shape of the simulated absorption spectra is produced based on the computed oscillator strengths of the electronic transitions and an empirically adjusted damping parameter or parameters that are functions of the resonance distribution profiles for these transitions. Usually the applied spectral line profiles are Gaussian, Lorentzian, or Voigt functions, but the choice might vary and be adjusted empirically. In the present studies, we applied a default strategy where oscillator strengths are computed at the PCM CIS level of theory and a Lorentzian spectral profile is parametrized by a single half-bandwidth  $\Gamma = 0.350$  eV, collective for all computed excitations. This strategy was also used to simulate the illustrative electronic absorption spectra and evaluate the weighting factors  $W_{\Gamma,s}$  to produce weighted gradients. In principle, the procedure might be improved further by introducing new or larger sets of damping parameters or applying a more accurate evaluation of oscillator strengths via quantum-mechanical or empirical adjustments.

### SCHEME 1: Structural Diagrams for the Imidazole and Histidine Derivatives and Tryptophan Included in the Computational Studies



### Illustrative Calculations

Both histidine and tryptophan side chains have been chosen to illustrate the computational effectiveness of the weighted-gradient approximation to predict resonance Raman intensity patterns. Examples of the imidazole ring and histidine are especially important since they provide a unique opportunity to test the computational power to predict the dramatic spectroscopic changes of RR signals observed when the ring is protonated or if the exchangeable protons are replaced by deuterium.<sup>4,5,12a,31</sup> Also, successful detection of the histidine environment by UVRR spectroscopy might greatly increase its applications to study enzyme active sites in which the histidine often plays a key role in catalytic activity.

The models of tryptophan and histidine in this study were built by cutting the residues at their backbone and replacing the C $\alpha$  atoms with a methyl –CH<sub>3</sub> group (Scheme 1). The models are chosen to avoid complications associated with rotational orientation of the side chain with respect to the plane of a peptide bond. This rotation is known to modulate some vibrational frequencies, such as the W<sub>3</sub> mode of tryptophan,<sup>31</sup> but these variations are not a focus of the present study.

**UV Absorption Spectra.** PCM CIS computed UV absorption spectral lines of tryptophan and various protonation states of the histidine ring in comparison with experimental data<sup>3,4</sup> are shown in Figure 1. As expected, the computed spectra are shifted toward higher frequencies due to the set of approximations within a chosen level of theory. Nevertheless, as it was pointed out above, the errors of computed excitation energies do not propagate to the computed RR intensities. Careful examination of computed electronic transitions and direct comparison with experimental UV spectra indicate that errors are quite systematic

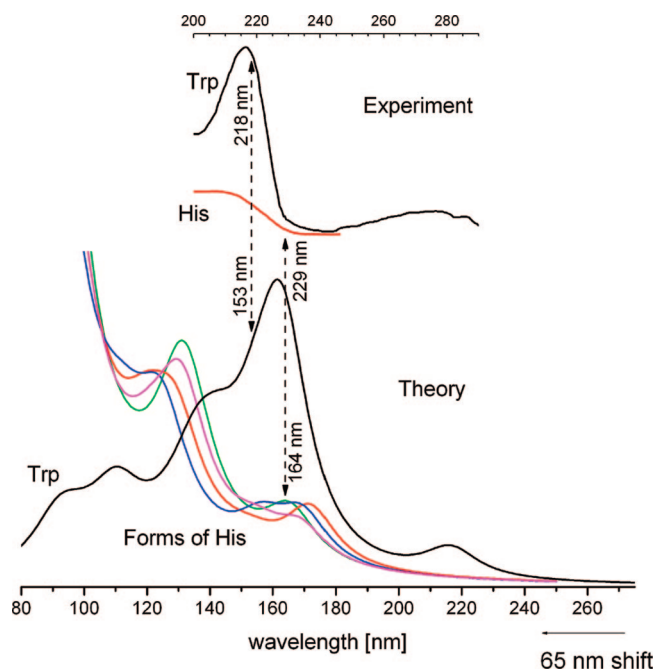


**Figure 1.** Calculated and experimental UV absorption spectra for tryptophan and histidine amino acids. Calculated spectra show four different forms of the histidine ring: His ( $\tau$ -isomer, red;  $\pi$ -isomer, magenta), His<sup>+</sup> (blue), and His<sup>-</sup> (green).

and easily corrected by a constant shift applied to a computed wavelength. It has been found that a 65 nm shift recalibrates the computed excitation wavelengths and places computed bands and patterns of tryptophan and histidine side chains, giving quite good agreement with experimental spectra. This simple correction implies that the experimental excitation at 229 nm used to measure imidazole and histidine UVRR spectra corresponds to a computed excitation at 164 nm, and the 218 nm excitation applied for tryptophan experimental spectra corresponds to a 153 nm computed wavelength, as indicated in Figure 1. It is worth mentioning that additional validation for the chosen calibration constant was achieved by examining the computed excitation profiles (not shown) for the characteristic vibrational bands of histidine and tryptophan models. These excitation profiles show maximal UVRR enhancements for histidine models around 164 nm and for a tryptophan model around 153 nm.

**UVRR Spectra of ImH and ImH<sub>2</sub><sup>+</sup>.** Understanding the nature of imidazole (ImH) and imidazolium cation (ImH<sub>2</sub><sup>+</sup>) RR bands, two biologically important forms of the side chain of histidine, has played a key role in searching for characteristic UVRR patterns of histidine in proteins. Experimental UVRR spectra with 229 nm excitation in aqueous solution for ImH and ImH<sub>2</sub><sup>+</sup> are compared with computed spectra in Figure 2. The intensity patterns show enhancement of in-plane ring modes consistent with resonance with the allowed  $\pi$ - $\pi^*$  electronic transition as a dominant factor. A characteristic pattern of decaying intensities of five bands for imidazole ring deformations in the 1200–1600 cm<sup>-1</sup> region is well reproduced in the computed spectrum. Starting with the most intense peak observed at 1259 cm<sup>-1</sup> and computed at 1283 cm<sup>-1</sup>, the pattern ends with the weakest band observed at 1534 cm<sup>-1</sup> and computed at 1562 cm<sup>-1</sup>. An enhancement pattern for the remaining bands observed in the lower frequency region, 900–1200 cm<sup>-1</sup>, is also well reproduced.

Protonation of the imidazole ring produces the cationic imidazolium ring and a dramatic perturbation of the RR spectrum. Only two strong bands now appear, observed at

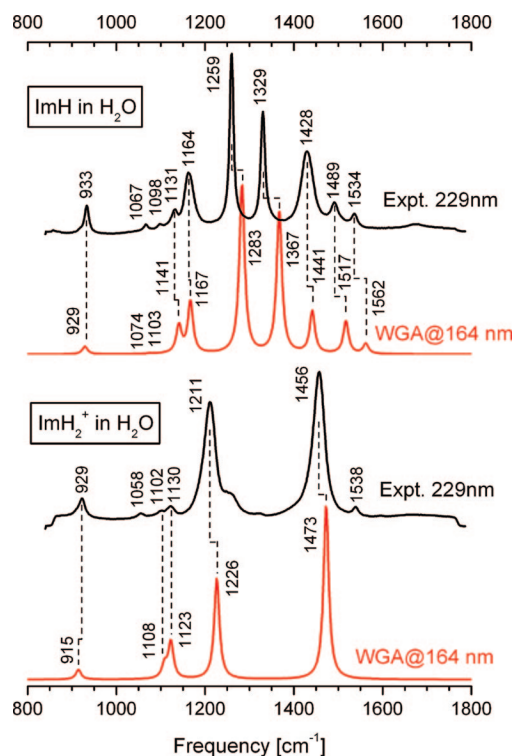


**Figure 2.** Calculated (red) by the weighted-gradient approximation and experimental (black) UVRR spectra for neutral imidazole (top two) and the cationic imidazolium form (bottom two).

around 1211 and 1456 cm<sup>-1</sup>. This dramatic simplification of the spectra is also well reproduced in the computed spectrum with two strong bands predicted at 1226 and 1473 cm<sup>-1</sup>. A few weaker features of the spectrum predicted at around 915, 1108, and 1123 cm<sup>-1</sup> are observed at 929, 1102, and 1130 cm<sup>-1</sup>. The overall agreement of predicted patterns with experiments is quite satisfactory, and all enhanced fundamentals might be easily assigned to observed bands. Computed frequencies are found to be slightly higher, which is expected due to limitation of the theory and the anharmonicity of vibrational modes. In principle, however, this minimal discrepancy could be easily adjusted empirically and by scaling the DFT force field.<sup>26</sup>

**UVRR Spectra of His, His<sup>+</sup>, and His<sup>-</sup>.** When the imidazole model of histidine side chain is extended to 4-ethylimidazole, four different protonation forms result: the two neutral tautomers in which either of the two nitrogen atoms are protonated and the imidazolium form and imidazolate form that are protonated and deprotonated at both nitrogen sites (Scheme 1). The absorption spectra for these forms show only minor changes, but their UVRR patterns are distinctly different. In addition, if exchangeable protons are replaced by deuterium, the intensity patterns undergo dramatic changes. In principle, these changes might be utilized for spectroscopic identification of tautomeric or protonated forms of histidine side chains in proteins. Figures 3, 4, and 5 show computed enhancement spectra of the four protonation forms of histidine in H<sub>2</sub>O and D<sub>2</sub>O compared to their experimental spectra with 229 nm excitation.<sup>7,31</sup> The comparison demonstrates quite good agreement of model spectra with experiment, allowing for unambiguous vibrational band assignments and identification of tautomer markers for neutral histidine (Figure 3). Some pairs of RR bands characteristic for the  $\tau$  and  $\pi$  tautomers are observed experimentally at 1587/1573, 1287/1265, and 1007/988 cm<sup>-1</sup> in H<sub>2</sub>O, have been previously identified by Ashikawa and Itoh<sup>32</sup> and are now confirmed in our modeling. However, their specific assignment

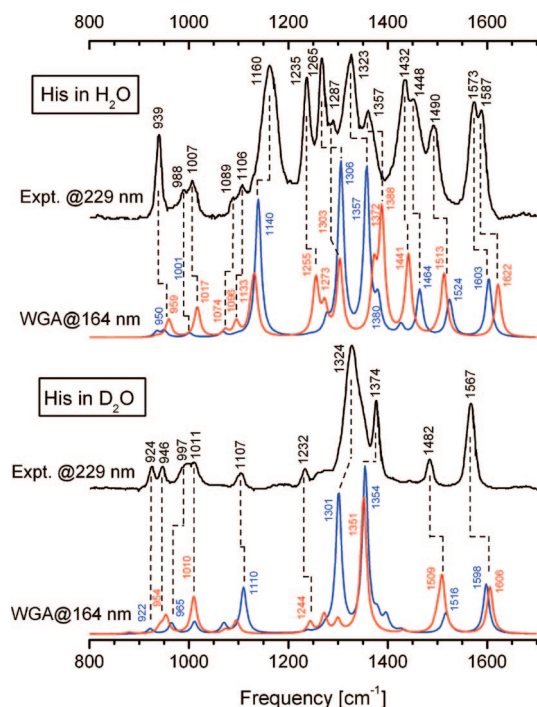


**Figure 3.** Calculated by the weighted-gradient approximation ( $\tau$  isomer in red and  $\pi$  isomer in blue) and experimental UVR spectra for the neutral histidine side chain (black) in  $\text{H}_2\text{O}$  (top three) and  $\text{D}_2\text{O}$  (bottom three).

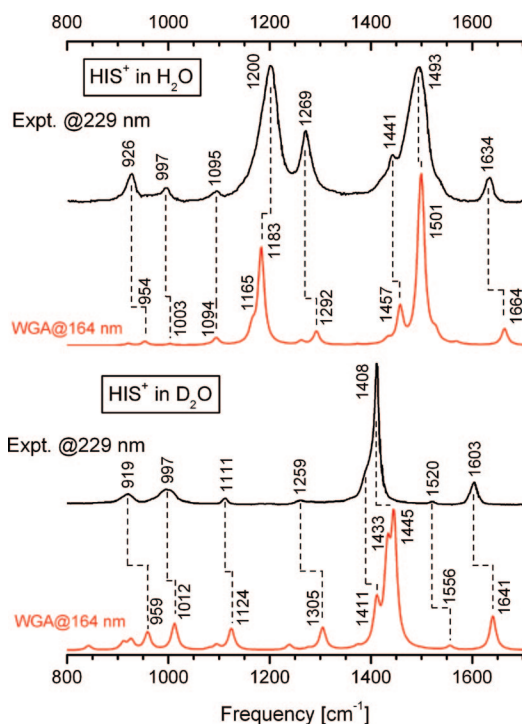


**Figure 4.** Calculated (red) by the weighted-gradient approximation and experimental (black) UVR spectra for the imidazolium form of the histidine side chain in  $\text{H}_2\text{O}$  (top two) and  $\text{D}_2\text{O}$  (bottom two).

of observed signals to specific tautomers is in disagreement with our models, which argue that the higher frequency in the pairs should be assigned to the  $\tau$  tautomer and not to the  $\pi$  tautomer as previously suggested.<sup>31</sup> This disagreement needs to be investigated more, but nevertheless, the overall agreement allows for full spectral assignment of the bands and the spectra–structure correlation. Interestingly, the deuterium substitution of the exchangeable protons in neutral histidine predicts quite different

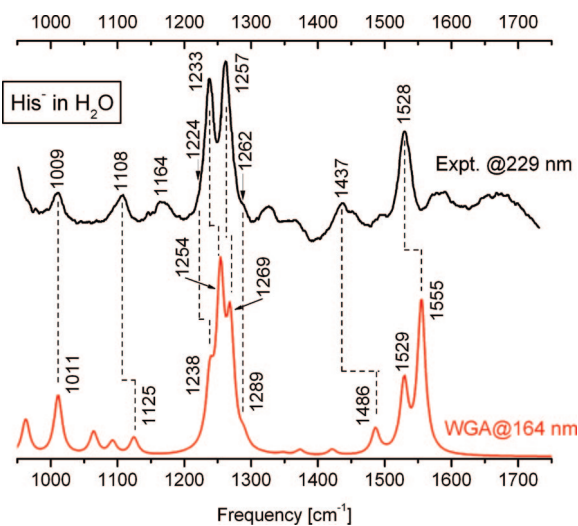


**Figure 5.** Calculated (red) by the weighted-gradient approximation and experimental (black) UVR spectra for the imidazolite form of the histidine side chain.

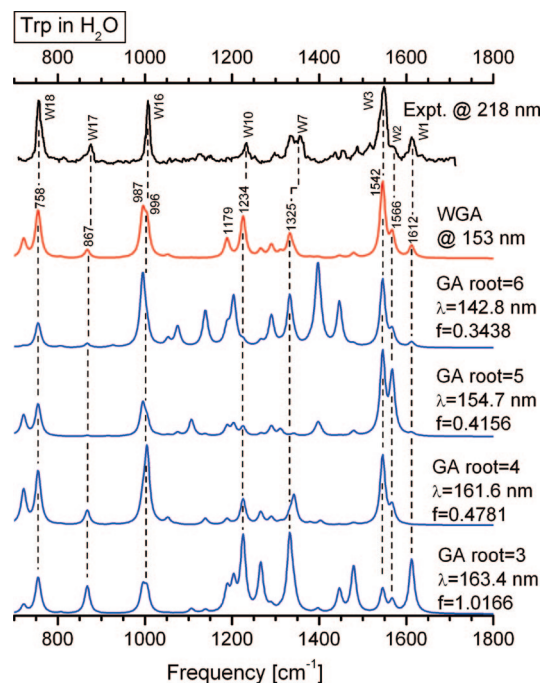


**Figure 6.** UVR spectra calculated by the weighted-gradient approximation (red) and gradient approximation (blue) within the particular single resonant state for the tryptophan side chain model and experimental (black) UVR spectrum for tryptophan amino acid.

intensity patterns for these tautomers, especially around 1250–1350  $\text{cm}^{-1}$ . The  $\tau$  tautomer shows only one intense band that is assigned to the observed band at 1374  $\text{cm}^{-1}$ , while the  $\pi$  tautomer gives two strong signals both of which are likely to contribute to the broad band observed at 1324  $\text{cm}^{-1}$ . Also, the band observed at 1107  $\text{cm}^{-1}$  is assigned to the  $\pi$  tautomer, while the band observed at around 1482  $\text{cm}^{-1}$  is dominated by the  $\tau$  tautomer.

Full protonation of 4-ethylimidazole reduces the number of isomers to one, and as expected, the 229 nm enhancement pattern is quite similar to those found for the imidazolium cation, but the spectra are slightly more structured due to the presence of the ethyl group. Again, computed spectra are able to reproduce the characteristic two strong signals observed at 1200 and 1493  $\text{cm}^{-1}$  with weaker features observed at 1634, 1441, 1269, 1095, 997, and 926  $\text{cm}^{-1}$ .



**TABLE 1: Selected Vibrational Frequencies for Tryptophan Model, Their Reduced Mass, and Effective Force Constants Along with Normalized Weighted Gradient Contributions of Particular Electronic Excitations**

gradient (mdyn) contributions to WG at 153 nm											
freq	$m$ (amu)	$k$ (mdyn/Å)	single states				sum of states			relative RR intensity	in-plane W assignment
			root = 3	root = 4	root = 5	root = 6	main	remaining	complete		
758.2	2.9537	1.0004	−0.0175	−0.0120	−0.0147	−0.0054	−0.0496	−0.0036	−0.0532	1835.1	W18
867.4	4.4101	1.9547	0.0210	0.0085	−0.0034	0.0030	0.0291	0.0012	0.0303	347.2	W17
987.4	1.4918	0.8569	0.0121	0.0059	0.0122	0.0077	0.0380	0.0041	0.0421	1747.2	W16
996.5	2.1372	1.2503	0.0138	0.0143	0.0094	0.0038	0.0414	0.0023	0.0437	1300.8	W15
1179.0	1.2391	1.0147	0.0115	0.0032	0.0067	0.0038	0.0253	0.0029	0.0282	787.4	
1234.3	1.6473	1.4786	0.0251	0.0082	0.0078	0.0022	0.0434	0.0058	0.0492	1728.7	W10
1324.7	2.3380	2.4173	−0.0312	−0.0055	0.0020	−0.0094	−0.0441	−0.0010	−0.0451	953.2	W7
1542.4	5.1503	7.2185	−0.0281	−0.0267	−0.0459	−0.0174	−0.1180	−0.0130	−0.1310	3133.6	W3
1565.6	5.5736	8.0489	−0.0210	0.0137	−0.0415	−0.0085	−0.0573	−0.0165	−0.0738	904.4	W2
1612.6	6.0419	9.2567	−0.0468	−0.0002	−0.0089	0.0053	−0.0505	−0.0081	−0.0586	511.4	W1

**TABLE 2: Normalized Weighting Factors (Percentage) for Four Main Electronic Transitions at a Particular Excitation Wavelength for Various Protonation Forms of Imidazole, Histidine, and Tryptophan Models**

at 164 nm	ImH	ImH <sub>2</sub> <sup>+</sup>	Im <sup>-</sup>	His(τ)	His(π)	His <sup>+</sup>	His <sup>-</sup>	at 153 nm	root	Trp
HOMO → LUMO	60.4	61.6	28.8	39.6	50.2	45.0	39.3	HOMO → LUMO+1	3	32.4
HOMO → LUMO+1	4.2	11.0	20.5	16.9	8.8	26.0	21.7	HOMO-1 → LUMO+1	4	18.1
HOMO-1 → LUMO	12.4	8.6	15.0	15.1	9.3	8.5	6.0	HOMO → LUMO+2	5	26.7
HOMO-1 → LUMO+1	3.6	2.6	11.7	2.8	2.8	1.9	9.9	HOMO-2 → LUMO	6	11.1
sum of contributions										
main	80.6	83.8	76.0	74.4	71.1	81.4	76.9	main		88.3
remaining	19.4	16.2	24.0	25.6	28.9	18.6	23.1	remaining		11.7

Upon substitution of exchangeable protons by deuterium, the spectrum of the imidazolium changes to give one prominent signal observed at around 1408 cm<sup>-1</sup> that is reproduced in calculations along with other observed weakly enhanced signals (see Figure 4). The UVRR spectrum of fully deprotonated 4-ethylimidazole is also well reproduced in calculations with characteristic intense structure of four fundamentals observed at around 1224, 1233, 1257, and 1262 cm<sup>-1</sup> and the band at 1528 cm<sup>-1</sup> (see Figure 5).

**UVRR spectra of Trp.** It has been demonstrated that the RR enhancement of tryptophan is a very responsive probe of hydrophobic and hydrogen-bonding interactions and a sensitive conformational marker in proteins. Therefore, successful modeling of intensity patterns of tryptophan upon resonant excitation could serve as an important benchmark for our study. A direct comparison of experimental spectra to computed spectra is presented in Figure 6. In this case, the DFT ground-state vibrational force field for the ethyl-indole model has been refined by the scaled quantum-mechanical (SQM) procedure<sup>26</sup> to demonstrate the effects of scaling. The agreement of a predicted spectrum using the weighted gradient approximation in combination with the SQM procedure with an experimental spectrum with 218 nm excitation<sup>31</sup> is excellent. All observed bands and their intensity patterns are well reproduced, with well-resolved signals of W<sub>3</sub>, W<sub>16</sub>, and W<sub>18</sub> bands that play a key role in probing the protein environment.

Figure 6 demonstrates the effects of the weighted-gradient approximation vs a standard single-state gradient approximation showing results when only a particular single state is taken into account. There are four excited states that have the largest contribution for the weighted gradient approach computed at 153 nm: root = 3, HOMO → LUMO+1 a transition computed at 163 nm with 32%, root = 4, HOMO-1 → LUMO+1 a transition computed at 162 nm with 18%, root = 5, HOMO → LUMO+2 a transition computed at 155 nm with 27%, and root = 6, HOMO-2 → LUMO a transition computed at 143 nm with 11% contribution. The remaining 12% comes from all other excitations but with significantly smaller individual contributions

to the weighted gradient. Nevertheless, when each of the four key resonant states is singled out to compute the resonance Raman spectral pattern, the experimentally observed pattern is not reproduced too well. Even though the excitation at 163 nm (root = 3) has the largest contribution at the amplitude level, the computed UVRR spectrum resulting from this state shows a large overestimation of intensity for W<sub>1</sub>, W<sub>7</sub>, and W<sub>10</sub> bands and underestimation for W<sub>2</sub>, W<sub>3</sub>, and W<sub>16</sub> as well as activation of other modes that are not prominent in the observed spectrum. In fact, none of the spectra computed with a single-state gradient approximation are capable of reproducing the experimental pattern as successfully as the weighted-gradient approach. This comparison clearly illustrates that the weighted-gradient approximation could easily correct for many common shortcomings and problems associated with prediction of resonance enhancements using a single-state gradient approach. Additionally, the gradients of key electronic states at 153 nm excitation along selected vibrational modes of the tryptophan model are listed in Table 1. The table illustrates the effect of gradient mixing at the amplitude level at which the resonant gradient contribution might add to enhance the intensity or subtract to weaken the intensity of a particular vibrational mode. RR intensities for most of selected modes of tryptophan are governed by gradients of four main resonant states with matching signs leading to gradient addition and increased intensities. However, gradients along W<sub>1</sub>, W<sub>2</sub>, W<sub>7</sub>, and W<sub>17</sub> modes indicate alternation of a sign leading to a gradient subtraction and reduced intensities. For instance, the intensity for the W<sub>7</sub> mode shows mainly gradient contributions with a positive sign where the largest contribution is from the HOMO → LUMO+1 electronic transition (root = 3). However, the effective intensity of the mode is weak since it is reduced by a negative gradient contribution from the HOMO → LUMO+2 electronic transition (root = 5). The same electronic transitions are key components for modulating the intensity for W<sub>17</sub> mode, however, in this case, most of the gradient contributions indicate a negative sign at the amplitude level that is counterweighted by a positive contribution from root = 5. Similarly, the intensity for the W<sub>2</sub>

mode is reduced due to a gradient sign alternation calculated for the HOMO-1  $\rightarrow$  LUMO+1 resonant transition (root = 4), and the intensity of the  $W_1$  mode is reduced due to a sign alternation of the gradient predicted for the HOMO-2  $\rightarrow$  LUMO transition (root = 6).

## Conclusions

The present study provides a basis for evaluating the electronic and vibrational factors that govern the Franck–Condon enhancement mechanism of resonance Raman active vibrations. The methodology utilizes the vertical gradients obtained from a manifold of computed electronic excitations to produce an effective weighted-gradient that is unique for a particular excitation wavelength. Therefore, unlike the specific-state gradient approach, this new approach allows for the effective quantum-mechanical estimation of spectral changes due to the excitation wavelength or the excitation profiles for particular vibrational modes. The efficiency of this procedure has been illustrated for biologically relevant chromophores and showed good agreement between observed and calculated RR spectra. Resonant enhancements resulting from the allowed  $\pi$ – $\pi^*$  electronic transitions were demonstrated by comparison of experimental with calculated URR spectra of histidine and tryptophan side chains. Interestingly, the controlled accessibility of the manifold of excited states by a resonant photon in the weighted-gradient approach provides an interesting assessment of enhancement conditions and an easy comparison to the single-state treatment. Table 2 lists the normalized distribution of weighting factors for key electronic transitions that resonate with a particularly chosen excitation wavelength: 164 nm for histidine models and 153 nm for a tryptophan model. The distribution demonstrates that for the ImH and ImH<sub>2</sub><sup>+</sup> models a single electronic transition (around 60% for the HOMO  $\rightarrow$  LUMO transition) strongly dominates and controls the calculated RR spectra, and indeed, previous single-state CIS prediction<sup>13a</sup> produced quite satisfactory results for these models. However, the single-state approach was not as adequate for other molecular systems presented here. As shown in Table 2, the Im<sup>–</sup> model requires as many as four key electronic transitions, all with significant contributions: (1) HOMO  $\rightarrow$  LUMO, (2) HOMO  $\rightarrow$  LUMO+1, (3) HOMO-1  $\rightarrow$  LUMO, and (4) HOMO-1  $\rightarrow$  LUMO+1. Similarly, “His” models demonstrate significant contribution from at least two or three excited states except for the His( $\pi$ ) tautomer which shows as much as 50% from the HOMO  $\rightarrow$  LUMO transition, and the tryptophan model requires at least four transitions (see above). As could be expected, a sum of normalized contributions from the main electronic transitions is averaging quite high, around 78% for histidine models (at 164 nm excitation wavelength) and 88% for tryptophan (at 153 nm excitation wavelength). Hence, failure to predict RR spectra for these systems is likely due to an insufficient single-state description to satisfy the requirement of inclusion of multiple states under these enhancement conditions.

The potential application of the weighted-gradient model to predict, identify, and analyze RR intensity patterns of metalloproteins, including toxic metals, is our immediate interest. In principle, however, it could provide a means to quantitatively and effectively analyze RR intensities and identify electronic and structural interactions occurring within the protein environment.

**Acknowledgment.** This work was supported by NIH grant S06 GM076168.

## References and Notes

- (1) (a) Carey, P. R. *Biochemical Applications of Raman and Resonance Raman Spectroscopies*; Academic Press: New York, 1982. (b) Parker, F. S. *Applications of Infrared, Raman and Resonance Raman Spectroscopy in Biochemistry*; Plenum: New York, 1983. (c) Spiro, T. G. *Biological Applications of Raman Spectroscopy*; Wiley-Interscience: New York, 1988; Vols. 1–3.
- (2) Harada, I.; Takeuchi, In *Spectroscopy of Biological Systems*; Clark, R. J. H., Hestler, R. E., Eds.; John Wiley & Sons Ltd.: Chichester, U.K., 1986; pp 113–175.
- (3) Rava, R. P.; Spiro, T. G. *J. Phys. Chem.* **1985**, *89*, 1856.
- (4) Caswell, D. S.; Spiro, T. G. *J. Am. Chem. Soc.* **1986**, *108*, 6470.
- (5) (a) Zhao, X.; Wang, X. J.; Spiro, T. G. *J. Am. Chem. Soc.* **1998**, *120*, 8517. (b) Zhao, X.; Wang, X. J.; Spiro, T. G. *Inorg. Chem.* **1998**, *37*, 5414.
- (6) Vargck, M.; Zhao, X.; Lai, Z. H.; McLendon, G. L.; Spiro, T. G. *Inorg. Chem.* **1999**, *38*, 1372.
- (7) Wang, D.; Zhao, X.; Vargck, M.; Spiro, T. G. *J. Am. Chem. Soc.* **2000**, *122*, 2193.
- (8) (a) Kozłowski, P. M.; Jarzecki, A. A.; Pulay, P. *J. Phys. Chem.* **1996**, *100*, 7007. (b) Kozłowski, P. M.; Jarzecki, A. A.; Pulay, P.; Li, X.-Y.; Zgierski, M. Z. *J. Phys. Chem.* **1996**, *100*, 13985. (c) Jarzecki, A. A.; Kozłowski, P. M.; Pulay, P.; Ye, B.-H.; Li, X.-Y. *Spectrochim. Acta A* **1997**, *53*, 1195. (d) Kozłowski, P. M.; Rush, T. S., III; Jarzecki, A. A.; Zgierski, M. Z.; Chase, B.; Piffat, C.; Ye, B.-H.; Li, X.-Y.; Pulay, P.; Spiro, T. G. *J. Phys. Chem. A* **1999**, *103*, 1357.
- (9) (a) Kramers, H. A.; Heisenberg, W. Z. *Phys.* **1925**, *31*, 681. (b) Dirac, P. A. M. *Proc. R. Soc. London, Ser. A* **1927**, *114*, 710. (c) Albrecht, A. C. *J. Chem. Phys.* **1961**, *34*, 1476.
- (10) (a) Lee, S.-Y.; Heller, E. J. *J. Chem. Phys.* **1979**, *71*, 4777. (b) Meyers, A. B.; Mathies, R. A.; Tannor, D. J.; Heller, E. J. *J. Chem. Phys.* **1982**, *77*, 3857. (c) Meyers, A. B.; Mathies, R. A. In *Biological Applications of Raman Spectroscopy*; Spiro, T. G., Ed.; Wiley-Interscience: New York, 1988; Vol. 2, Chapter 1, pp 1–58. (d) Myers, A. B. *J. Raman Spectrosc.* **1997**, *28*, 389.
- (11) (a) Hizhnyakov, V.; Tehver, I. *Phys. Status Solidi* **1967**, *21*, 755. (b) Tonks, D. L.; Page, J. B. *J. Chem. Phys. Lett.* **1979**, *66*, 449. (c) Page, J. B.; Tongs, D. L. *J. Chem. Phys.* **1981**, *75*, 5694. (d) Tongs, D. L.; Page, J. B. *J. Chem. Phys.* **1982**, *76*, 5820.
- (12) (a) Markham, L. M.; Mayne, L. C.; Hudson, B. S.; Zgierski, M. Z. *J. Phys. Chem.* **1993**, *97*, 10319. (b) Rush, T.; Kumble, R.; Mukherjee, A.; Blackwood, M. E., Jr.; Spiro, T. G. *J. Phys. Chem.* **1996**, *100*, 12076. (c) Billingham, B. E.; Loppnow, G. R. *J. Phys. Chem. A* **2006**, *110*, 2353.
- (13) (a) Jarzecki, A. A.; Spiro, T. G. *J. Raman Spectrosc.* **2001**, *32*, 599. (b) Jarzecki, A. A.; Spiro, T. G. *J. Phys. Chem. A* **2005**, *109*, 421. (c) Neugebauer, J.; Baerends, E. J.; Efremov, E. V.; Ariese, F.; Gooijer, C. J. *J. Phys. Chem. A* **2005**, *109*, 2100. (d) Jensen, L.; Schatz, G. C. *J. Phys. Chem. A* **2006**, *110*, 5973. (e) Herrmann, C.; Neugebauer, J.; Presselt, M.; Uhlemann, U.; Schmitt, M.; Rau, S.; Popp, J.; Reiher, M. *J. Phys. Chem. B* **2007**, *111*, 6078.
- (14) Petrenko, T.; Neese, F. *J. Chem. Phys.* **2007**, *127*, 164319.
- (15) (a) Guthmuller, J.; Champagne, B. *J. Chem. Phys.* **2007**, *127*, 164507. (b) Mennucci, B.; Cappelli, C.; Cammi, R.; Tomasi, J. *Theor. Chem. Acc.* **2007**, *117*, 1029.
- (16) Duschinsky, F. *Acta Physicochim. URSS* **1937**, *7*, 551.
- (17) Jensen, L.; Zhao, L. L.; Autschbach, J.; Schatz, G. C. *J. Chem. Phys.* **2005**, *123*, 174110.
- (18) Herzberg, G.; Teller, E. Z. *Phys. Chem.* **1933**, *B21*, 410.
- (19) Manneback, C. *Physica* **1951**, *XVII*, 1001.
- (20) Van Labeke, D.; Jacon, M. *J. Chem. Phys. Lett.* **1975**, *34*, 160.
- (21) Savin, F. A. *Opt. Spectrosc.* **1965**, *19*, 555.
- (22) Warshel, A.; Dauber, P. *J. Chem. Phys.* **1977**, *66*, 5477.
- (23) Champion, P. M. In *Biological Applications of Raman Spectroscopy*; Spiro, T. G., Ed.; Wiley-Interscience: New York, 1986; Vol. 3, pp 249–292.
- (24) Frisch, M. J.; Trucks, G. W.; Schlegel, H. B.; Scuseria, G. E.; Robb, M. A.; Cheeseman, J. R.; Montgomery, J. J. A.; Vreven, T.; Kudin, K. N.; Burant, J. C.; Millam, J. M.; Iyengar, S. S.; Tomasi, J.; Barone, V.; Mennucci, B.; Cossi, M.; Scalmani, G.; Rega, N.; Petersson, G. A.; Nakatsuji, H.; Hada, M.; Ehara, M.; Toyota, K.; Fukuda, R.; Hasegawa, J.; Ishida, M.; Nakajima, T.; Honda, Y.; Kitao, O.; Nakai, H.; Klene, M.; Li, X.; Knox, J. E.; Hratchian, H. P.; Cross, J. B.; Bakken, V.; Adamo, C.; Jaramillo, J.; Gomperts, R.; Stratmann, R. E.; Yazyev, O.; Austin, A. J.; Cammi, R.; Pomelli, C.; Ochterski, J. W.; Ayala, P. Y.; Morokuma, K.; Voth, G. A.; Salvador, P.; Dannenberg, J. J.; Zakrzewski, V. G.; Dapprich, S.; Daniels, A. D.; Strain, M. C.; Farkas, O.; Malick, D. K.; Rabuck, A. D.; Raghavachari, K.; Foresman, J. B.; Ortiz, J. V.; Cui, Q.; Baboul, A. G.; Clifford, S.; Cioslowski, J.; Stefanov, B. B.; Liu, G.; Liashenko, A.; Piskorz, P.; Komaromi, I.; Martin, R. L.; Fox, D. J.; Keith, T.; Al-Laham, M. A.; Peng, C. Y.; Nanayakkara, A.; Challacombe, M.; Gill, P. M. W.; Johnson,



B.; Chen, W.; Wong, M. W.; Gonzalez, C.; Pople, J. A. *Gaussian 03*, Revision C.02; Gaussian, Inc.: Wallingford, CT, 2004.

(25) Cossi, M.; Scalmani, G.; Rega, N.; Barone, V. *J. Chem. Phys.* **2002**, *117*, 43–54.

(26) (a) Rauhut, G.; Pulay, P. *J. Phys. Chem.* **1995**, *99*, 3093. Rauhut, G.; Pulay, P. *J. Phys. Chem.* **1995**, *99*, 14572. (b) Baker, J.; Jarzecki, A. A.; Pulay, P. *J. Phys. Chem. A* **1998**, *102*, 1412.

(27) Zerner, M. C. In *Reviews of Computational Chemistry*; Lipkowitz, K. B., Boyd, D. B., Eds.; VCH: New York, 1991; Vol. 2, p 313.

(28) Foresman, J. B.; Head-Gordon, M.; Pople, J. A.; Frisch, M. J. *J. Phys. Chem.* **1992**, *96*, 135.

(29) Roos, B. O. *Ab Initio Methods in Quantum Chemistry*; Wiley: New York, 1987.

(30) Marques, M. A. L.; Nogueira, F.; Rubio, A.; Burke, K.; Ullrich, C. A.; Gross, E. K. U. *Time-Dependent Density Functional Theory*; Springer: Berlin, 2006.

(31) Takeuchi, H. *Biopolymers (Biospectroscopy)* **2003**, *72*, 305.

(32) Ashikawa, I.; Itoh, K. *Biopolymers* **1979**, *18*, 1859.

JP8095715